Università Cattolica del Sacro Cuore
Sede di Brescia
Facoltà di Scienze Matematiche, Fisiche e Naturali
Corso di Laurea di Secondo Livello in Fisica

Development of an asynchronous optical sampling laser system for time-resolved reflectivity measurements on high temperature superconductors

Relatore:
Dott. Gabriele Ferrini
Correlatore:
Dott. Claudio Giannetti

Laureando: **Isabella Avigo**
mat. 3611051

Anno Accademico 2009/2010

Contents

Chapter 1

Introduction

In this work we present an asynchronous optical sampling laser system and its development to perform reflectivity time-resolved pump-probe measurements on high temperature superconductors (HTSC). The system we employed in our measurements is called ASOPS (Asynchronous Optical Sampling) and it consists in two mod-locked coupled twin fiber lasers of two different colors delivering pulsed laser radiation at 1560 nm and 780 nm. The repetition rate is 100 MHz, tunable in frequency hence allowing to perform of experiments with pump-probe technique. In comparison with the conventional pump-probe technique, ASOPS has a decisive advantage since it does not require the use of a mechanical delay stage and enables the sampling of the complete time window of 10 ns ($T = \frac{1}{100MHz}$). This peculiar feature turned out to be a powerful tool in our measurements, since beside already known fast dynamics occurring in HTSC, on the picosecond time scale, we had the possibility of sampling a much longer relaxation dynamics tackling other interesting phenomena occurring in the system at longer time scales (hundreds of picoseconds).

Time-resolved spectroscopies offer appealing perspectives for the investigation of strongly correlated systems, since they give access to the dynamical excitation and relaxation of electrons close to the Fermi level.

Despite high-temperature superconductivity represents one of the most interesting problem within the physics of correlated systems, the mechanism at the base of this phenomenon remains an open issue and is object of a strong debate among scientific community. The superconductivity with the highest critical temperature was found in compounds belonging to the family of copper oxides (cuprates). The feature common to all cuprates is given by two dimensional CuO_2 planes weakly interacting with the neighboring planes containing other atoms, like Ba, La, Bi, acting like charge reservoir to dope with holes or electrons the CuO plane.

Our goal is to investigate HTSC with different concentrations of dopant carriers to understand how the out-of-equilibrium behavior is affected by the doping. In the chapter 2 we will outline the problem of the electron-phonon coupling in cuprates introducing the electron-phonon coupling strength constant λ, which play a fundamental role in the relaxation dynamics of standard metals. Whether the strength of λ is high enough to account for HTSC is an issue not yet clarified.. We will then introduce time-resolved spectroscopy as an effective tool to investigate HTSC dynamics and extract λ.

In chapter 3 we will describe more in detail our samples (BSLCO), introducing some structural properties and equilibrium optical properties. We will then introduce non-equilibrium optical properties triggered by an external stimulus coming from a laser pulse and two useful models used to extract the constant λ from a pump-probe measurement. The two temperature model was largely employed in the case of metals while a recent extension of this model is the three temperature model employed in HTSC studies. This is the model we used to analyze our experimental data and extract λ.

In chapter 4 and 5 we will describe in detail the ASOPS system (ch. 4) with all its features and differences with respect to the conventional systems, we will then describe the characterization of the laser and the optical set up built to perform our measurements (ch. 5).

In chapter 6 we will present our experimental data and analysis, divided in fast dynamics and slow dynamics. Fast dynamics include the first part of our 10 ns measurement, i.e. a few picoseconds (1 ps=10^{-12} s), and bring information on the electron-phonon coupling mechanisms responsible for the thermalization between the electrons kicked out of equilibrium by the pump pulse and the lattice (or a particular subset of vibrational modes). The slow dynamics occur after the previous ones and consist in an oscillatory dynamics lasting some tens of picoseconds overlapped to the slow exponential dynamics describing the relaxation of the lattice temperature toward the temperature of the thermal bath (300 K).

In chapter 7 we will discuss our results and discuss them for different concentrations of dopant carriers in order to show how the doping affects the non-equilibrium physics of HTSC.

Chapter 2

Electron-Phonon coupling in Cu-O based high-T_c superconductors

In this chapter we discuss some interesting features of high temperature superconductors (HTSC), with a particular attention to the role of the doping carriers concentration in the electron-phonon coupling constant λ. We will then introduce time-resolved spectroscopy technique as a tool to investigate HTSC properties and directly measure λ.

2.1 Problems and open issues

In high temperatures superconductors the copper oxygen planes play a fundamental role because the $Cu - O$ orbitals within these planes form the electronic bands close to the Fermi level. Below a critical temperature T_c electrons in these planes overcome the Coulomb repulsion, forming a condensate of Cooper pairs characterized by a macroscopic coherence length. Among the different issues still controversial about high-Tc superconductivity, one of the most important points is whether the mechanism at the base of the formation of the Cooper pairs is similar to that occurring in conventional superconductors. Within the Bardeen-Cooper-Shrieffer theory (BCS) of conventional superconductivity, the glue responsible for the formation of the Cooper pairs is given by the phonons through a weak effective potential acting among electrons near the Fermi level. The first generalization of the BCS theory in the case of strong electron-phonon coupling has been carried on by Eliashberg and it takes into account the retardation effects of the phonons response. The main physical quantity of this theory is the glue function $\alpha^2F(\Omega)$. $F(\Omega)$ being the phonon density of states, Ω the phonon frequency and $\alpha^2(\Omega)$ the strength of the frequency dependent electron-phonon interaction. The electron-phonon coupling constant λ provides the strength of the coupling integrated over the phonon frequencies:

$$\lambda = 2\int \frac{\alpha^2F(\Omega)}{\Omega}d\Omega \tag{2.1}$$

The critical temperature depends on λ and in the strong coupling regime this dependence is given by in the following expression

$$T_c = \frac{\tilde{\Omega}}{1.2}\exp\left[-\frac{1.04(1+\lambda)}{\lambda - \mu^*(1+0.62\lambda)}\right] \tag{2.2}$$

where $\tilde{\Omega}$ is the characteristic phonon frequency and is defined as an average over $\alpha^2F(\Omega)$:

$$\tilde{\Omega} = \langle\Omega^2\rangle^{\frac{1}{2}} = \left[\frac{2}{\lambda}\int_0^\infty \Omega\alpha^2F(\Omega)d\Omega\right]^{\frac{1}{2}} \tag{2.3}$$

This formalism is not restricted to the case of phononic interactions but it can also be applied to a more general bosonic interactions.

Studies performed on conventional superconductive metals[2] shows that, accordingly to eq.(2.1), T_c increases with the increasing of λ. We report in table below critical temperature values for corresponding λ in the case of few common superconductive metals[2]:

	λ	T_c
V	0.80	0.9K
Nb	1.16	1.06K
Pb	1.45	1.2K

If these considerations were valid for high-T_c materials, we should expect values of λ around several units (i.e. $\lambda = 6.25$) for high values of T_c (i.e. around 30K) while all scientific studies performed until now shows that in HTSC the values of λ are similar to those of common metals and even lower[9][7]. These results demonstrate that λ is not the only glue which leads to the formation of cooper pairs, many other complex aspect come into play and the BCS theory is not sufficient to explain the mechanisms leading to the Cooper pair formation in HTSC. These compounds are characterized by a strong electronic correlation, hence the band theory, relying on the independent-electron approximation, does not account for the complex phase diagram (see fig.2.1) of these compounds in which the superconductive state is only one of multiple aspects.

2.2 Phase diagram and role of the doping

The physical properties of HTSC crucially depend on the nature of the dopant carriers (electrons or holes) and on their concentration. In fig. (2.1) we sketch the phase diagram of a hole doped HTSC, showing the different phases as a function of the temperature and of the dopant concentration p. Let us

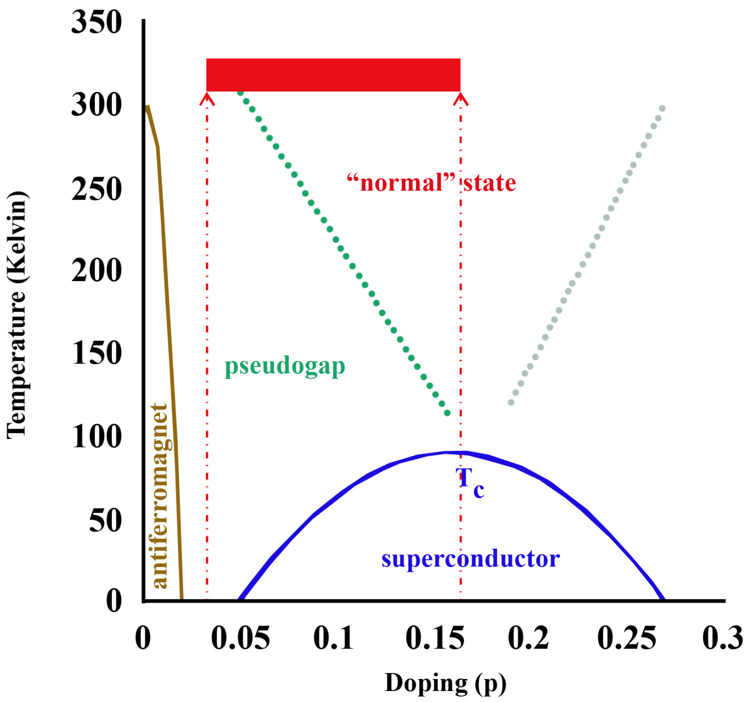

Figure 2.1: Figure taken from[7].Phase diagram of an hole doped cuprate. The red zone shows the range of the measurements reported in this work

consider the undoped compound La_2CuO_4: the valence of Cu is 2+, leading to a $3d^9$ electronic configuration of copper atoms. The crystal field that originates from the interaction with the four planar oxygens surrounding the copper atom and the out of plane oxygens (apical oxygens) breaks the degeneracy of the d-levels leading to the splitting into four occupied low energy orbitals (with symmetry xy, xz, yz, $3z^2 - r^2$) and one half-filled high energy orbital $x^2 - y^2$[7]. According to the band theory this compound should be a metal but experimental findings indicate that it is an insulator with a large gap (2 eV) where the spins of the Cu holes are coupled antiferromagnetically. This configuration, displaying a band gap between bands of like characters (between the two coppers), is called *Mott-insulator* while a *charge transfer insulator* presents a band gap between copper and oxigen. The failure of the band theory comes from its inability to include the dramatic effects of the strong electronic correlations.

This fact can be worked out by adding other atoms through the $Cu - O$ layers (like La, Ba, Sr), that is adding dopant carriers (electrons or holes). With the increasing of doping concentration, the electronic properties of the compound changes, gradually leading to a diminution of the gap introducing a transition to a conductive behavior and, in the case of optimal doping, a superconductive behavior with a critical temperature trend significantly affected by the concentration of the dopant carriers.

Our measurements span the red zone of the phase diagram, from the Mott-insulator zone, to the superconductive phase in correspondence of optimal doping, with the main goal of measuring λ for different doping level. In particular, we had two underdoped samples with different carriers concentration and one optimally doped. Their features and properties will be discussed in chapter 2.

2.3 Time-resolved reflectivity measurement technique to investigate HTSC

Among different experimental techniques to investigate non-equilibrium properties of HTSC, time-resolved spectroscopy performed with pump-probe is an effective tool to temporally resolve the dynamics of the electronic excitations out of equilibrium and to provide important information on the mechanisms of the energy exchange with other degrees of freedom of the system. In this configuration, a pump pulse of energy $\hbar\omega$ excites all the electrons that occupy the electronic bands in a spectral region that extends $\hbar\omega$ below E_F causing variations in the reflectivity properties of the system. The monochromatic probe pulse, delayed of a time τ with respect to the pump pulse, follows the carriers relaxation dynamics in a time window which is inversely proportional to the repetition rate of the system. Through and experimental pump-probe measurement, it is possible to obtain a profile of the reflectivity variation $\Delta R/R$ of the system induced by the pump pulse

$$\frac{\Delta R}{R} = \frac{R_{exc} - R_{eq}}{R_{eq}} \tag{2.4}$$

Where R_{eq} is the reflectivity of the system at the equilibrium and R_{exc} is the non-equilibrium reflectivity which occurs when the system is photoexcited by the pump pulse. In the case of metals and HTSC, the relaxation time is inversely proportional to the electron-phonon coupling.

When the pump pulse excite the sample, the optical properties of the systems changes, leading to a sharp variation of the reflectivity (or transmittance). The system then relaxes to equilibrium and the probe pulse follows this process in time. An example of a typical ΔR profile is shown in fig. (2.2).

Progress in the field of time-resolved reflectivity measurements techniques, led to the formulation of many models and techniques to extract information on the significant quantities involved in a peculiar process from the $\Delta R/R$ profile. We will now report two models which have been largely used in the study of metals and HTSC to extract the electron-phonon coupling strength λ and other quantities of interest.

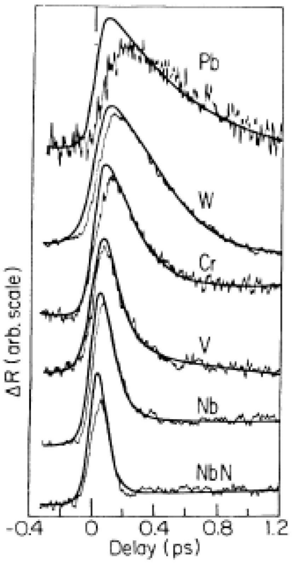

Figure 2.2: fig. taken from [2], pump-probe measurements and numerical fits of ΔR for various metal.

2.3.1 Two temperature model

In time-resolved optical experiments an ultrafast laser pulse (pump pulse, ~100 fs) excites the electronic carriers above the Fermi level E_F while a second delayed pulse monitors the evolution of the system back to the initial equilibrium state. In the case of metals, electrons are excited from occupied to non-occupied states above the Fermi level E_F and then thermalize, through inelastic scattering processes, on a characteristic timescale of few femtoseconds. The electron-electron thermalization occurs in a time $\tau_{e-e} \sim \frac{\hbar E_F}{2\pi E^2} \sim 4$ fs for electrons excited at 0.5 eV above E_F that is significantly faster compared to the pulse temporal width. Since τ_{e-e} is much shorter than the period of the typical phonon modes, the electronic system, in this time interval, is not coupled to the lattice and reaches a temperature T_e higher than the phonon bath temperature T_{ph}. The final value of the temperature T_e depends on the pulse energy and is larger than T_{ph} because the heat capacity of the electrons is much smaller than the lattice heat capacity. After the thermalization, the excited electrons start to loose energy through electron-phonon scattering processes and relax towards the states near the chemical potential. A first model providing a simple formula to derive the thermal relaxation time in metals was developed by Allen[1] and it is called the two temperature model (2TM). He obtained a simple expression of the electron-phonon relaxation time τ_{e-ph} in terms of T_e (electronic temperature), the mean square phonon frequency $\langle\omega^2\rangle$ and λ:

$$\tau_{e-ph} = \frac{\pi k_b T_e}{3\hbar\lambda\langle\omega^2\rangle} \tag{2.5}$$

Allen's model represents an interesting method that allows to derive λ more directly than other experimental techniques. In fact τ_{e-ph} can be obtained fitting $\Delta R/R$ to an exponential decay while $\langle\omega^2\rangle$ is taken from the literature or can be approximated by $\omega_D^2/2$. The 2TM model has been successfully applied to different metals obtaining a λ that ranges between 0.05 and 0.15 in agreement with the data obtained by other experimental techniques. This formalism has been employed also in HTSC in normal state, where the system seems to have a pseudo-metallic behavior: the λ extracted from transient reflectivity measurements was found to increase to 0.82 in the case of $Bi2212$ superconductor[2] ($Bi_2Sr_2CaCu_2O_{8+\delta}$). Further development in the investigations of HTSC led to the development of other models, one of these being the three temperature model.

2.3.2 Three temperature model

Very recently time-resolved photoemission spectroscopy on cuprates has been performed by L. Perfetti et. al.[9]. In this experiment the sample is excited by an ultrashort infrared pulse (1.5 eV) while a second delayed pulse (6 eV) probes the transient electron distribution $f(\omega,\tau)$ by photoemitting electrons along the nodal direction. The temperature evolution $T_e(\tau)$ of the excited electron population is directly extracted fitting a Fermi-Dirac distribution at temperature T to $f(\omega,\tau)$ at different delay times. Two different dynamics of the extracted electronic temperature where observed and interpreted assuming that excited electrons first thermalize with a first subset of more strongly interacting phonons including a limited number of modes and, once the hot electrons and hot phonons reach a common temperature, they all thermalize with the rest of the cold lattice via a residual scattering with the lattice modes. The first process occurs in some hundreds of femtoseconds and hot phonons dissipate their energy by means of anharmonic decay, while the last process occurs in few picoseconds yielding a longer exponential decay (hundreds of picoseconds) in the reflectivity dynamics.

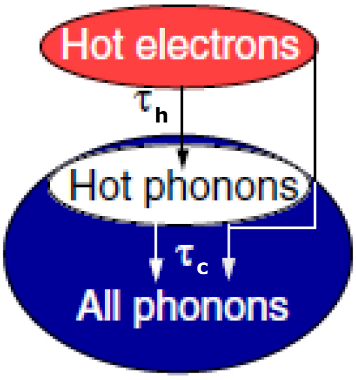

Figure 2.3: fig. taken from [9], Sketch of the energy transfer during the relaxation process.

Quantitative insight on the relative number and coupling strength of the nonequilibrium phonons is obtained by solving an extended version of the 2TM. Accordingly to the 2TM the rate of energy transfer between electrons and phonons is related to the electron-phonon coupling function $\alpha^2F(\Omega)$

through the integral:

$$\left(\frac{\partial E_e}{\partial t}\right)_{e-ph} \propto \int_0^\infty \Omega^2 \alpha^2 F(\Omega)(n_e - n_p) d\Omega \tag{2.6}$$

where n_e and n_p are the Bose-Einstein distributions respectively:

$$n_e = \frac{1}{e^{\frac{\Omega}{k_b T_e}} - 1} \qquad n_p = \frac{1}{e^{\frac{\Omega}{k_b T_p}} - 1} \tag{2.7}$$

The spectral density of phonons is simplified considering only one phonon mode Ω_0 between 40meV and 70meV, i.e., $F(\Omega) = \delta(\Omega - \Omega_0)$. These modes are coupled to the electrons through λ by eq. (2.1). The rate equations of the 3TM are:

$$\frac{dT_e}{dt} = -\frac{3\lambda\Omega_0^3}{\hbar\pi k_b^2}\frac{n_e - n_p}{T_e} + \frac{P}{c_e} \tag{2.8}$$

$$\frac{dT_p}{dt} = \frac{c_e}{c_p}\frac{3\lambda\Omega_0^3}{\hbar\pi k_b^2}\frac{n_e - n_p}{T_e} - \frac{T_p - T_l}{\tau_\beta} \tag{2.9}$$

$$\frac{dT_l}{dt} = \frac{c_p}{c_l}\frac{T_p - T_l}{\tau_\beta} \tag{2.10}$$

P is the energy density exciting the system, the specific heats of electrons, hot phonons and rest of the lattice are:

$$c_e = \gamma T_e \qquad c_p = 3f\Omega_0 \frac{\partial n_p}{\partial T_p} \qquad c_l = 3(1-f)\Omega_0 \frac{\partial n_p}{\partial T_p} \tag{2.11}$$

Where γ is the linear heat-capacity coefficient and the parameter f indicates the fraction of total modes that are more strongly coupled. Electron-phonon scattering with the $(1-f)$ lattice modes that are more weakly coupled barely contributes to the temporal evolution of T_e and therefore has been neglected. The decay time τ_β describes the anharmonic decay of hot phonons. We report below a table with the results[1] obtained in ref.[9] by fitting the temporal profile of T_e with the numeric solution of eq. (2.8):

$\Omega_0[meV]$	T_l	f	$\lambda\Omega_0[meV^2]$	$\tau_\beta[ps]$
40	30 ± 10	$0.13 - 0.25$	$300 - 380$	2 ± 0.1
70	300 ± 10	$0.18 - 0.25$	$340 - 380$	0.9 ± 0.1

In the particular case of our samples, we used this model to fit our data in order to obtain λ, τ_β and f for optimally doped (x=0.4) and underdoped (x=1, x=0.8) $Bi_2Sr_{2-x}La_xCuO_6$ (BSLCO) hence tackling the question of the dependence of these quantities on the dopant concentration.

---

[1] these results refer to optimally doped $Bi - 2212$

Chapter 3

Structural and optical properties of BSLCO

The Bismuth Strontium Lantanium copper oxide is a Bi-based cuprate with a single CuO_2 layer (the key structural element common to all HTSC) per unit cell and it represents a very good candidate for important considerations about systematic doping-dependent studies. In particular BSLCO is suitable for the normal state analysis because it displays relatively low critical temperature (T_c max $\sim$ 30 K). High quality $Bi_2Sr_{2-x}La_xCuO_6$ (BSLCO) single crystals can be reliably produced over a wide range of carrier concentrations. The hole doping is controlled by replacing Sr with La, larger La concentration x corresponds to smaller hole doping per copper ion, p, and the relation between x and p has been sorted out by F.F. Balakirev et al.[11](Cfr also[10]). In BSLCO, p decreases for increasing x according to a well known[10] relation which is not linear, due to compensation effects.

The accessible hole doping range spans the underdoped Mott-insulator limit, through the superconductive phase and the overdoped regime(as shown in fig. 2.1). It was found that optimum doping (i.e. the doping corresponding to the maximum T_c) occurs at $p_{opt} \sim 0.16$ (which is achieved with $x \sim 0.4$), and that the superconductivity disappears in the underdoped materials at $p \sim 0.10$ ($x \sim 0.8$). The sample we considered in our measurements were Bismuth Strontium Lantanium copper oxide ($Bi_2Sr_{2-x}La_xCuO_6$) crystals at three different doping levels and we investigated their optical properties in the normal state (i.e. at room temperature).

Measurements of reflectivity variation of BSLCO can be performed with Asops technique to extract information on the electron-phonon coupling mechanism. Hence, the comprehension of the behavior of the optical properties of the system as the doping is changed is mandatory for the data analysis.

3.1 Equilibrium optical properties

Optical spectroscopy measurements provide the real and imaginary part of the dielectric function which describes the material response to an external excitation from a light pulse:

$$\epsilon(\omega) = \epsilon_1(\omega) + i\epsilon_2(\omega) = \epsilon_1(\omega) + i\frac{4\pi\sigma_1(\omega)}{\omega} \tag{3.1}$$

where $\sigma_1(\omega)$ is the real part of the optical conductivity and ω is the frequency of the electromagnetic incident radiation. The real part ϵ_1 brings information on the phase velocity of the incident wave in the material, while the imaginary part ϵ_2 is correlated to the optical conductivity and thus takes into account dissipative effects.

Moreover, the dielectric function is also related to the refractive index through

$$\epsilon(\omega) = \tilde{n}^2(\omega) = n^2(\omega) + ik^2(\omega) \tag{3.2}$$

It is then possible to relate the the real and imaginary parts of the refractive index and the dielectric function:

$$\epsilon_1 = n^2 - k^2, \qquad \epsilon_2 = 2nk \tag{3.3}$$

and

$$n = \frac{\sqrt{|\epsilon| + \epsilon_1}}{2}, \qquad k = \frac{\sqrt{|\epsilon| - \epsilon_1}}{2} \tag{3.4}$$

The reflectivity, in case of normal incidence is given by:

$$R = \frac{(n^2 - 1) + k^2}{(n^2 - 1) - k^2} \tag{3.5}$$

Besides this general considerations, let us consider a superconductor. In this case the electric conductivity is infinite and this leads to the appearance of a δ at zero frequency in the optical conductivity, as we can see from the London equation:

$$\sigma(\omega) = \frac{\pi}{2}\left(\frac{n_s e^2}{m^*}\delta(0)\right) + \sigma_{reg} \tag{3.6}$$

where n_s is the superconductive electron density, m^* the effective mass and σ_{reg} is the contribution of normal electrons, described through a Drude-Lorentz model. The integral over $\sigma(\omega)$ over all frequency is called *spectral weight*, it obeys to the sum rules and it is related to the total density of electrons interacting with the electromagnetic wave:

$$8\int_0^\infty \sigma_1(\omega)d\omega = \frac{4\pi n e^2}{m_e} \tag{3.7}$$

The presence of a $\delta(0)$ has the effect of shifting the spectral weight from 0 frequency to finite frequency during the transition of the system from the superconductive state to the normal state. In particular, it was demonstrated that in HTSC an anomalous variation of the optical spectral weight, involving transitions at energy as high as 2 eV [Molegraaf Science], underlies the onset of superconductivity, strongly affecting the reflectivity in the infrared/visible range. These facts have consequences on the reflectivity of the system.

In this work we are going to present experiments consisting in a study of the reflectivity variation of the system, therefore it is useful to get information both on the reflectivity spectrum of the system and on the penetration length. This last quantity is necessary to the volume of sample photoexcited by the laser.

Studies on the equilibrium optical conductivity of BSLCO have been conducted by S. Lupi et al.[10] with ARPES[1]. From their data we were able to extract the penetration length(fig.3.1) and the reflectivity (fig3.2) of our samples as function of the energy at $T = 300K$ and for different dopings

From this graph we can observe that the penetration length almost double for underdoped compounds with respect to the optimally doped. The penetration length was necessary to calculate the energy density delivered to the system by the absorption of the pump pulse:

$$\frac{E}{V} = \frac{P}{rep.rate} \cdot \frac{1}{2\pi r_s l_p} \tag{3.8}$$

Where P is the incident power, the rep. rate is 100 MHz, and r_s is the spot radius evaluated in $10 \mu m$.

In fig.3.2 we report the the trend of the reflectivity as the doping is changed. It is clear from the graph that the plasma frequency ω_p (dashed orange lines) drifts with the doping. The plasma frequency ω_p is proportional to the total

---

[1] angle resolved photoemission spectroscopy

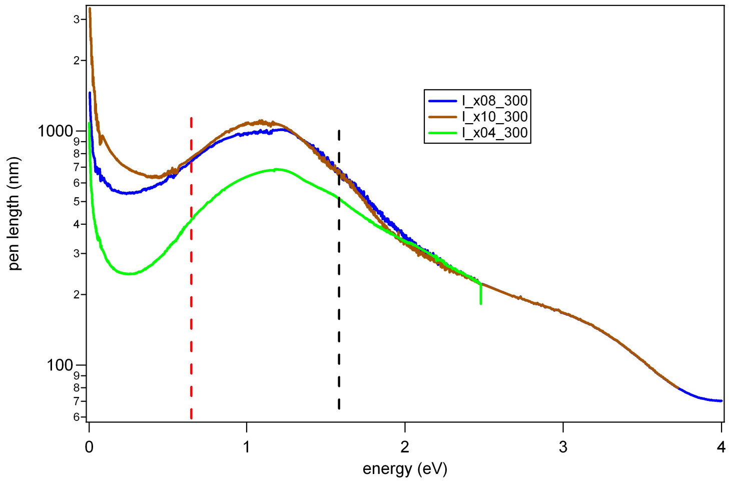

Figure 3.1: The dashed red and black lines mark the pump and probe photon energy respectively (0.8eV and 1.6eV)).

number of free charge carriers in the system N:

$$\omega_p = \frac{4\pi N e^2}{m} \tag{3.9}$$

e and m being the electron charge and mass respectively. In the case of underdoped compounds, the total number of carriers decreases leading a decreasing of the plasma frequency value. From the classical Drude model, the real part of the dielectric function is given by:

$$\epsilon_1 = 1 - \frac{\omega_p}{\omega^2 - \Gamma} \tag{3.10}$$

A decreasing of the plasma frequency caused by the presence of different doping affects the dielectric constant and therefore is translate in changes in the reflectivity.

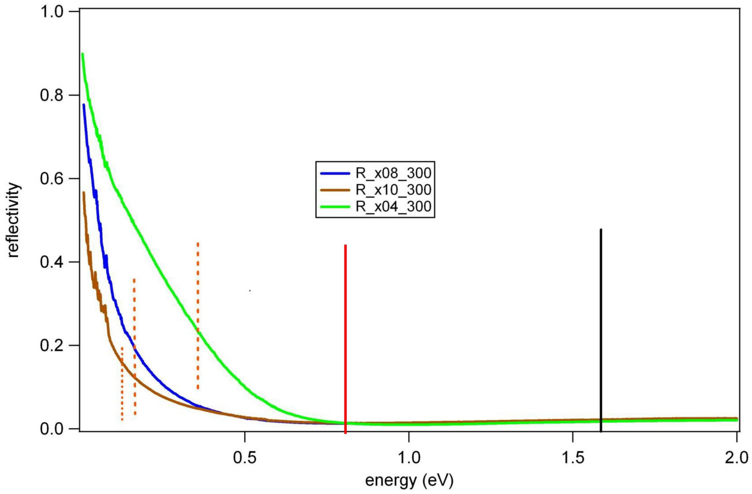

Figure 3.2: Reflectivity of the three samples are shown. From the graph it is clear that for fixed energy, the reflectivity increases with the doping. The dashed orange lines mark the correspondent plasma frequency ω_p, the red and black lines mark the mean pump and probe energy respectively.

3.2 Non-equilibrium optical properties

The mechanisms responsible of an HTSC system response to a laser pulse stimulus haven't been completely sorted out yet as the band theory which is valid for metals is no more valid for HTSC because of the strong correlation among the electrons.

3.3 Normal state

The normal state refers to the state of the compound at room temperature (T=300 K), see Fig. 2.1.

We know that changes in the reflectivity signal are strongly related to the dependence of the dielectric function on the temperature T through the Fermi-Dirac distribution. In metals, after the arrival of the pump pulse, the electron temperature rises, causing the tails of the Fermi distribution to spread out and leading to the depletion of previously occupied states below E_F and to the occupation of previously empty levels above E_F. These states then absorb photons from the probe pulse which experiments a corresponding increase in absorption. Thus changes in T_e will cause changes in R. Change in the reflectivity can also occur due to the lattice temperature changes. For example band shifting arising from thermal strain will cause R to change. Ones the pump pulse excites the compound, changes in the reflectivity occur due to both electron and lattice temperature. We can then assume:

$$\Delta R = a\Delta T_e + b\Delta T_l \tag{3.11}$$

where we supposed, similarly to the case of metals(see [2]), that ΔR were proportional to both electron and lattice temperature, a and b being two proportional constant. After extracting T_e and T_l from the three temperature model, one can obtain the decay time of the relaxation dynamics and the electron-phonon coupling constant λ. So far, the parameter λ has been determined by different experimental techniques i.e. inelastic neutron scattering, optical conductivity, ARPES and tunneling spectroscopy but with contrasting results ranging from a weak coupling regime ($\lambda \sim 0.1$) to a strong coupling regime ($\lambda \geq 1$). All these techniques allow to extract the electron-boson coupling through a complex procedure of inversion of the experimental data. The constant λ is finally obtained by integration of the coupling function over the boson frequencies up to a given cutoff frequency. The peculiarity of time-resolved measurements lies in the possibility to directly extract the coupling constant λ from the experimental data in the time domain.

Contrary to the standard equilibrium techniques it is possible to disentangle the contribution of different bosons on the base of the different relaxation dynamics. We said in the former section that the doping affects the equilibrium reflectivity of the system through a shifting of the plasma frequency. Obviously this fact affects also the $\Delta R/R$ signal (see eq.2.4. Since, in our experiments, we always probe at 1.6 eV, for different samples we see different contribution to the reflectivity: the ΔR signal is higher in the case of optimal doping $x = 0.4$ than for underdoped sample $x = 0.8$. For what concern the sample with $x = 1$, we see a negative signal in ΔR. Therefore, the drift of the plasma frequency ω_p with the doping p could lead to a dual effect: first of all, this shift causes, according to the Drude model, the contribution to the total heating to decrease, leading to the lowering of the ΔR peak maximum; secondly, for very underdoped compounds, intraband effects occur and can overcome the Drude effects resulting in a possible increasing of ΔR but with negative sign.

3.4 Superconductive state

Time-resolved reflectivity measurements performed on HTSC under T_c reveal some important differences as compared to metals, concerning the slowing of the relaxation dynamics below T_c(the decay time increases of about one order of magnitude) and a substantial increase in the $\Delta R/R$ signal with respect to metals [7]. A phenomenological description of the photoinduced non-equilibrium dynamics of superconductors is given by the Rothwarf-Taylor equations (RT model). The RT model consists in two coupled differential equations describing the temporal evolution of a quasiparticles system[2], created by the laser-induced breaking of Cooper pairs, followed by the process of recombination into the condensate. The process of recombination is me-

---

[2] quasiparticle refers to a phenomena whose behavior is characterized as that of a single particle in a system, including the effect the particle has on the system. It can be roughly defined as the combination of a particle and its influence on the local environment.

diated by the emission of a boson at the same energy of the superconductive gap[7].

One of the outstanding problems connected to the origin of HTSC is to determine which are the bosons mediating the formation of Cooper pairs. In particular, the determination of the electron-boson coupling strength λ allows to shine light on the mechanism of pairing.

Chapter 4

Pump-probe spectroscopy with ASOPS and system overview

4.1 Comparison between standard pump-probe technique and ASOPS technique

In time-resolved pump-probe experiments an ultrafast laser pulse triggers a reaction and a second pulse, delayed against the pump pulse, takes a snapshot of the induced change. The stimulated process can then be followed in time providing a picture of the dynamics we want to study. In a typical pump and probe line, both pump and probe pulses are originated from the same laser source. The original laser beam is splitted into two beams going through different paths and encountering to the sample surface. The probe pulse is delayed by changing its optical path with a mechanical sliding stage, this position change is translated into a change of the time delay between pump and probe pulse by $\Delta t = \Delta x/c$ (c being the light speed).

Although this scheme has been widely used over the past decades it nevertheless has some disadvantages: The maximal deviation range of mechanical delay stages is usually limited to few centimeters. Therefore, the maximal time delay is on the order of some ten to hundred picoseconds. Obviously the realization of time windows on the order of nanoseconds is unpractical with this technique.

Secondly, the signal at every position of the delay line has to be sampled individually. During the movement of the delay line no sampling is possible. This leads to very long data acquisition times, on the order of minutes up to hours. Moreover, exact alignment of the optical beam path including the mechanical delay line is mandatory. Even slight misalignments or deviations due to the mechanical properties of the delay stage will cause false changes of the signal on the detector leading to wrong experimental results.

ASOPS system (**AS**ynchronous **OP**tical **S**ampling) obviates the need for a mechanical delay line and allows high-speed scanning over several nanoseconds of time delay without moving parts. Time resolution below 100 fs can be reached. This all-optical sampling method is based on two femtosecond lasers with slightly different but stabilized pulse repetition rates. The repetition rate of the first laser (called pump laser) is slightly offset from the repetition rate of the second laser (called probe laser) by a fixed offset frequency Δf. The following equation is always valid:

$$f_{probe} = f_{pump} - \Delta f \qquad \Delta f \ll f_{pump} \tag{4.1}$$

If the pulses of both lasers are emitted simultaneously at the time t_0, the following pulses at the time t_1 are separeted by:

$$\tau = \frac{1}{f_{pump}} - \frac{1}{f_{probe}} = \frac{|f_{probe} - f_{pump}|}{f_{pump} f_{probe}} \approx \frac{\Delta f}{f_{pump}^2} \tag{4.2}$$

the third couple of pulses will be delayed by 2τ and so on until they are again emitted simultaneously at the time $1/\Delta f$. This way the time window $T = 1/f_{pump}$ is sampled with a resolution of τ within a time $1/\Delta f$.

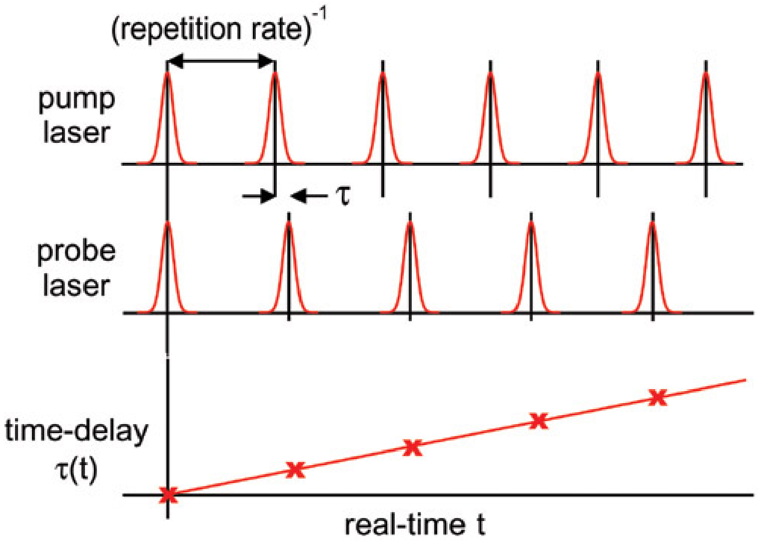

Figure 4.1: scheme of pump and probe pulses rate

4.2 C-fiber ASOPS system

The system we employed in our measurements is a Twin-C fiber ASOPS system, made by Menlo System. It's composed by two femtosecond twin mode-locked fiber lasers (called laser A and laser B). The laser resonator is a fiber ring. The light pulses that circulates in the fiber ring are amplified in an erbium-doped fiber and the energy requested for amplification is fed from multiple semiconductor laser diodes. Part of the laser resonator is the mode-lock controller, its setting determine if the laser operates mode-locked (pulses) or in the continuous wave mode. The mode-locked controller is set such that the laser operates mode-locked.

The model C-fiber has a built in amplifier for the pulses from the laser. The light pulses are polarized at the input (by a polarization controller), then amplified in the fiber and finally they're splitted (by a polarized beam splitter) at the output into two beams with linear polarization (fig.4.2). Both laser outputs have 100MHz repetition rate, which means a 10ns measurable time window.

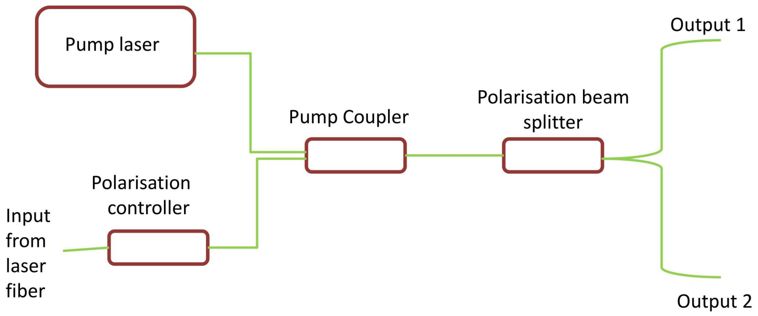

Figure 4.2: Amplifier schematic

Laser A has a wavelength output of 1560nm and an output power of about 180mW. In laser B the second harmonic of Laser A is generated with a periodically poled non linear crystal giving light at 780 nm. On principle not all the light at 1560 nm can be completely converted into light at 780 nm, therefore both wavelength leave the crystal and a subsequent dichroic mirror separates them, so that each one is available at its output(fig.4.3).

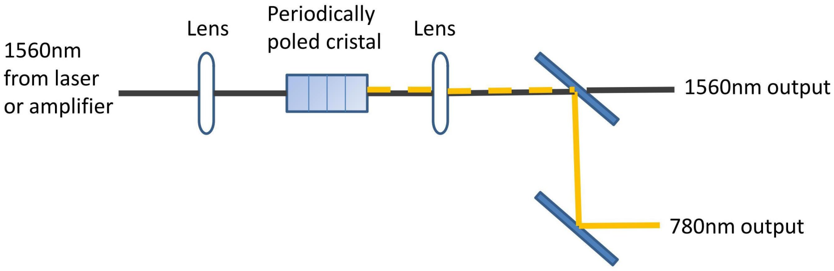

Figure 4.3: second harmonic generation and subsequent separation of the two beams

The output power of laser B is about 90 mW and its repetition rate is tunable in frequency in order to supply the desirable time delay for the sampling. In principle, the repetition rate offset tuning range can be tuned between 0.1 Hz and several tens of kHz, actually the use of all those offset frequencies is unpractical: the number of acquired points increases with the reduction of detuning but this leads to a very long acquisition time and the measure will be affected by changes due to the timing jitter and the timing shift of the trigger signal. If we compare two single measurement obtained integrating 20000 single scans at $\Delta f = 1kHz$ and $\Delta f = 10Hz$ we obtain a resolution (considering only the laser resolution) of $\frac{10^3Hz}{10^16Hz^2} = 100fs$ and $\frac{10Hz}{10^16Hz^2} = 1fs$ respectively, but the acquisition time needed is about 20 s in the first case and more than 10 minutes in the second case. Hence, the acquisition of a signal with a very high laser resolution and an elevated number of points would be unaffordable. On the other hand if the detuning offset frequency is too elevated, the number of acquired points will dramatically decrease leading to a loss of information and also a loss in resolution. Therefore we mainly settled at some tens or hundreds of Hertz (from 30Hz to 200Hz) of offset detuning frequency for acquiring short acquisition time windows (few picoseconds) and around 1 kHz for long acquisition time windows (untill 10 ns).

Depending on the sign of Δf both lasers can be used as either pump or probe laser. In our experiment we used the 1560nm cavity as the source for the pump pulse and the 780nm cavity as probe.

After manually setting the detuning (Δf), a feedback system acts in the electronics of the laser to keep it locked.

The repetition rate of both lasers is detected by a photo diode (PD) and filtered by an appropriate RF-bandpass filter(BP). The filtered photo diode signals are mixed (M) with the signal of a fixed frequency oscillator running at 980 MHz (PLO). The resulting 20 MHz signal are either mixed with a fixed 20MHz signal (frequency doubled 10 MHz reference oscillator)

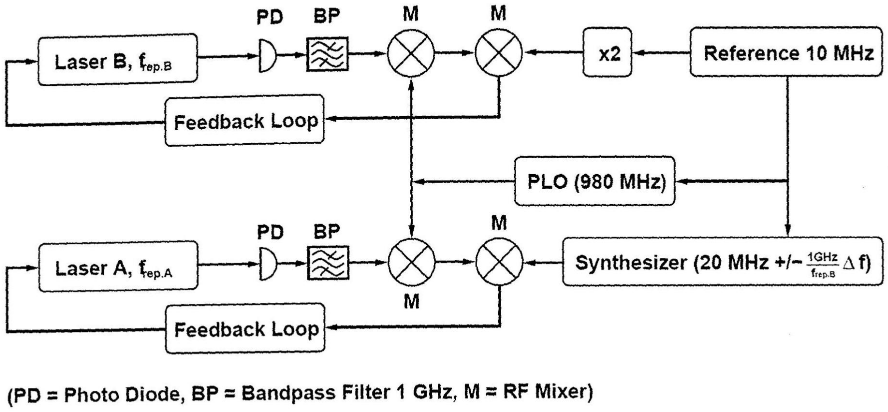

Figure 4.4: feedback system overview

or with the tunable signal from a digital synthesizer running at 20MHz $\pm$ $(1\mathrm{GHz}/f_{rep.B}) \cdot \Delta f$(laser A). The generated signals are used as an error signals for the feedback loop controllers that regulate the repetition rate of both lasers. In figure (4.4) a scheme of the feedback system is represented.

In the laser heads an end mirror is mounted on a piezoelectric transducer fixed on an integrated stepper motor. By changing the position of the mirror, the cavity length can be varied, which results in a change in the repetition frequency of the emitted laser pulses. The stepper motor is used to coarsely set the repetition rate, and the piezo is used for fine-tuning and locking.

The value of the rep. rate difference Δf is set by the user keeping into account all the previous consideration.

Chapter 5

General set up description and characterization

As outlined in the previous chapter, Asops techniques allows to perform a time-resolved optical sampling experiment on on a time window of 10 ns with femtoseconds time resolution with no drawbacks coming from a mechanical delay stage.

It is important to point out that even if a 10 ns time window is available, many phenomena (like the ones will be discussed in this chapter) have a duration of hundreds of femtoseconds, 5 order of magnitude shorter. Though it is not necessary to acquire the whole time window, a small percentage (0.2%-0.3%) of it is optimal.

Therefore it is important to communicate to the acquisition board the moment when the event to be measured occurs. For this aim a trigger signal taken from the laser oscillator is connected to the oscilloscope and to the digitizer. Moving a handle integrated in the synthesizer, the phase can be adjusted and the trigger signal synchronized with the signal we want to measure.

The development of this system for our measurement on HTSC required some preliminary stages: first of all the construction of a transmission line and the characterization of the lasers pulses, obtained studying the autocorrelation of both pump and probe pulses. Then the construction of a reflection optical line and its characterization performing some preliminary measurements on HOPG (Highly Ordered Pyrolytic Graphite). In this chapter we will deal with the description of all these aspects.

5.1 Pulse characterization

In pump and probe techniques, two slightly asynchronous lasers pulses hit the sample exactly at the same point on its surface. All the information can be extracted when there is both spatial and temporal coincidence on the sample. It is then clear that a first step in performing a pump and probe experiment is to evaluate the duration of the convolution of pump and probe pulses. For this aim we used a type I BBO crystal to generate the sum pulse and we were interested in its full width at half maximum (FWHM).

Another fundamental step is to evaluate the broadening of this sum pulse due to the timing jitter and to the trigger shift in time.

Figure 5.1 represents a simplified scheme of the optical line built to perform these measurements.

The light coming from both lasers is directed using a series of mirrors (M) on a first lens (100 mm focal length) that focuses the two beams on a type I BBO (thickness 0.5 mm). We obtained spatial coincidence by making the two beams both passing through a $75\mu m$ pinhole put in the crystal holder, then replaced with the crystal itself. Once the crystal is rotated and the phase matching angle is found, the sum pulse of 520 nm is produced, the signal is detected by an avalanche photodiode (APD) and the gaussian signal is visible on-line on the oscilloscope. This signal is very clear on the oscilloscope, and we used it as reference to synchronize the trigger signal from the laser.

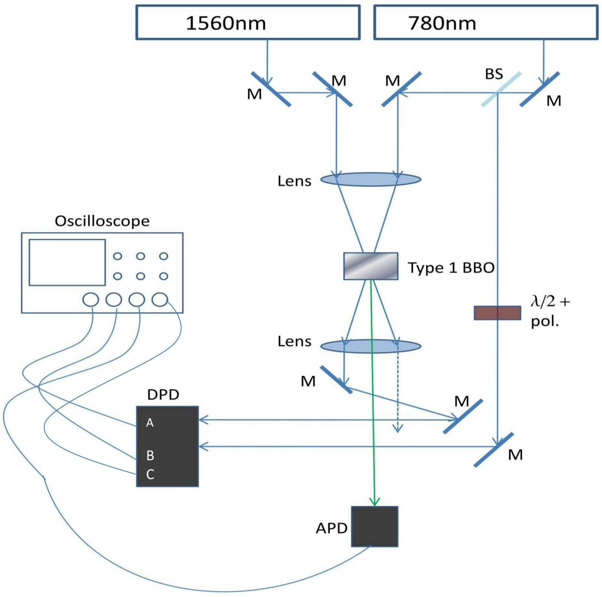

Figure 5.1: schematic optical line for sum pulse production

After the first mirror, the probe pulse passes through a beam splitter (BS) which transmits 70% and reflects 30% of the beam. The transmitted part of the probe pulse reaches the crystal and interacts with the pump to produce the sum pulse then it passes through a second lens (identical to the previous one) placed 10 cm from the crystal and using two mirrors it is directed to a differential photodiode (DPD, 100MHz bandwidth). The reflected probe pulse acts like a reference signal, it follows a different path and reaches the DPD without undergoing the interaction with the pump. A combination of a polarizer plus a $\lambda/2$ waveplate is placed on this path.

After their interaction in the nonlinear crystal, the pump pulse and the probe pulse undergo a depletion because part of their energy is employed in the sum production. This small (in comparison to the background noise of the pump signal) depletion signal can also be detected once we remove the background, and can be acquired with the acquisition board. This signal has the same temporal duration of the sum pulse.

The DPD has two integrated fast photodiodes (labeled with input - and input +), it collects the two different probe signals, one in the input - and the other in the input +, and displays their difference at the output. Using the combination polarizer plus $\lambda/2$ glass it is possible to adjust the reference probe signal varying its intensity (without polarization changing) and compensate the difference with the probe signal coming from the crystal. With this procedure, the background almost vanishes and the small depletion signal can be acquired.

5.1.1 ASOPS measurements of pulses autocorrelation and depletion

We performed measurements of the probe depletion in two different ways:

- EXTERNAL TRIGGER: we set the source of the trigger external. Because of the jitter, the acquisition board 'sees' all the singular gaussians oscillating around t_0 (t_0 being the center of the gaussian). This leads to a broadening of the signal width.
- AUTOTRIGGER: we set the source of the trigger signal on the gaussian. In this way, all the successive gaussians are centered exactly at the same time t_0 and the gaussian width results being the real one, not affected by the timing jitter.

In both cases we obtained our best measurements mediating a large number of acquisitions (10,000) with a PCI-5922 digitizer (15MHz, 16 bits).

The difference between the FWHM measured in the first way and the FWHM measured in the second way, allows us to estimate the signal broadening due to the timing jitter.

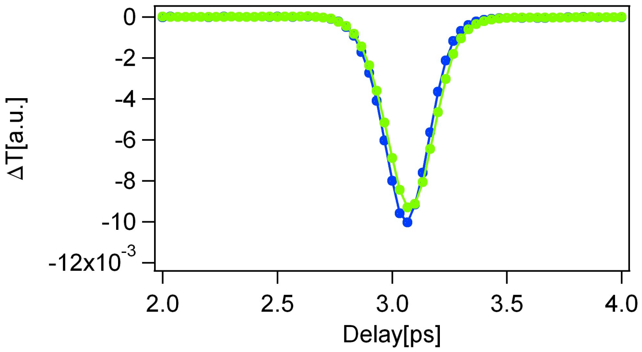

Figure 5.2: depletion signal acquired with external trigger (green) and with autotrigger (blue)

Our measurements are plotted in the graph (fig.5.2). All acquisition settings are reported in table below.

Δf	50 Hz
Sample rate	15 MS/s
N° acquired points	10,000
perc. of scan	0.03%
laser resolution	5 fs
PCI 59922 resolution	33.3 fs
acquisition time	

The percentage of scan corresponds to a time window of 9,966.67 fs, the laser resolution is given by [4.2], and the acquisition board resolution is given by $\frac{Df}{Samplerate \cdot rep.rate} = 50Hz\frac{10ns}{15MHz} = 33.3fs$.

Fitting our experimental data with a gaussian function, we could evaluate the FWHM of both the depletion signals.

Our fitting function was:

$$f(t) = y_0 + Aexp\left[-\left(\frac{t-t_0}{w}\right)^2\right] \tag{5.1}$$

inverting this formula to obtain $FWHM = 2(t - t_0)$, we have:

TRIGGER	w [fs]	FWHM [fs]
external	148.98 ± 0.75	248.1 ± 0.9
auto	139.72 ± 0.85	232.6 ± 1

Which means that the temporal broadening in our signal acquired with external trigger is 15.5 fs every $\left(\frac{n^{\circ} scan}{\Delta f}\right) = \left(\frac{8000}{50}\right) = 160$ seconds.

5.2 Optical set up

Performing the autocorrelation of the laser pulses caused us to construct a transmission optical line, at least a rudimental one. We then had to improve our optical set up in order to perform our measurements on BSLCO completing our optical transmission branch and realizing an optical reflection branch. In this section we will deal with a detailed description of our set up and of all optical components. We will then report some acquisition tests on HOPG which we used to characterize our reflection line.

5.2.1 description of the complete optical set up

We focused our attention in the realization of a set up which could enable the user to both transmission and reflection measurements with the minimal perturbation of the line. We also constructed an additional optical line in order to make the trigger positioning simpler and faster. In order to simplify our description we will consider two lines separately:

- **Sample line**: this line describes the paths of pump and probe laser beams directed on the sample and then reaching the detector after being transmitted or reflected.
- **Trigger line**: this line describes the paths of part of the two lasers beam reaching a type I BBO nonlinear crystal in order to produce a sum frequency of the 1560nm and 780nm beams. This signal at 520nm is detected by the APD as described in the previous chapter.

The purpose of building a trigger line besides the line we employ in the experiment is to make as fast as possible the operation of trigger positioning in our 10 ns time window. As mentioned in the previous section, we want to study very fast dynamics in comparison with the available time window, this leads us to select a $10^4 - 10^5$ shorter time window and communicate to the digitizer (PCI-5922) when starting the sampling acquisition via an external trigger signal. It is useful to constantly keep the sum (or depletion) signal on-line on the oscilloscope as a reference signal. The signal detected on the sample line is much smaller (even 3 order of magnitude)than the sum signal, hence it is impossible to check it on the oscilloscope. We can then synchronize the trigger signal with the sum signal once we have synchronized the latter with the first. Therefore we constructed the Sample line and the Trigger line requesting that the optical path differences between pump and probe beams were the same in each branch. From $\Delta t = \Delta x/c$ (c being the speed of light and Δx the optical path difference), we have that if Δx_1 and Δx_2 are equal, then the sum signal detected by the APD at the end of the trigger line and the signal detected by the DPD at the end of the sample line will occur at the same time. We coarsely achieved this goal by measuring the distances between subsequent optical elements while placing them on the optic bench and we obtained a fine adjustment using a micrometric translator strategically placed under a mirror in the Trigger line.

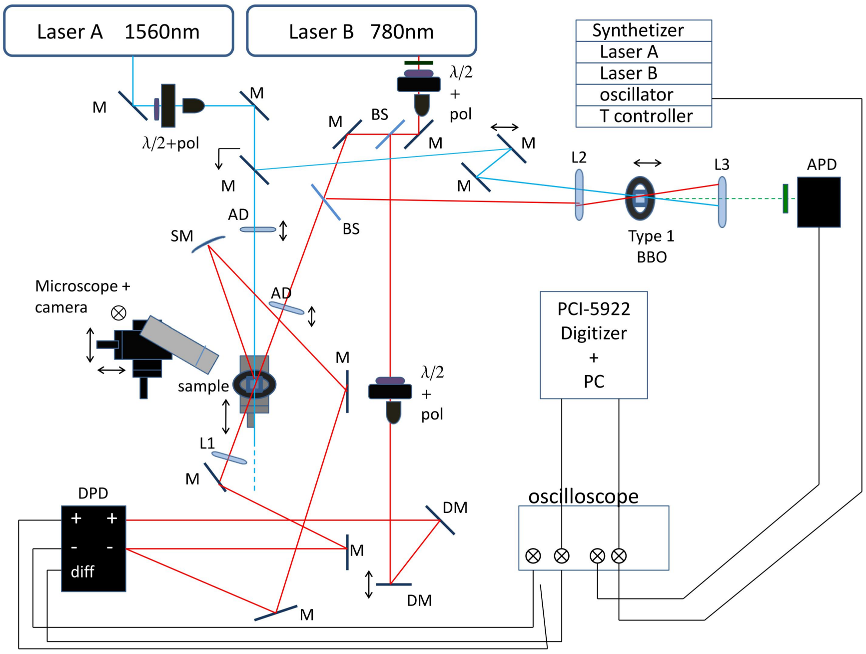

Figure 5.3: Complete scheme of all optical lines

A complete scheme of our set up is represented in fig 5.3.

SAMPLE LINE: The pump laser beam at 1560 nm (0.8 eV) first passes through a $\lambda/2$ waveplate mounted on a rotator and through a polarizer. This combination allows the user to modify a laser beam intensity in a continuous way without affecting its polarization. Using a series of both metallic and dielectric mirrors the beam is directed towards the sample and focused on its surface by a 100 mm focal length achromatic doublet. The probe laser beam at 780 nm (1.6 eV) passes through a combination of $\lambda/2$ waveplate plus polarizer, a first beam splitter (BS) is placed after the first mirror (M) and divides the beam into two parts. 70% of the beam is transmitted and directed towards the sample using a series of both metallic and dielectric mirrors. This beam portion is focused on the sample surface by a 50 mm focal length achromatic doublet. 30% of the beam reflected from the BS is directed to an input channel of the DPD without previous interaction with the pump pulse on the sample. On this path another combination of $\lambda/2$ waveplate plus polarizer is placed. Similarly to what we did for the depletion signal detection described in the former chapter, this beam acts as a reference probe beam.

The position of the two beams on the sample is monitored using a microscope ending with an infrared digital camera. (devo spiegare qui, la procedura per trovare la coincidenza spaziale o posso spiegarla nel cap successivo?)

After the pump and the probe beams encounter on the sample surface, they interact and the probe beam, must be recollected. The probe signal can be transmitted through the material, in this case the beam is parallelized through a 50mm focal length lens, then directed to another input channel of the DPD using a series of metallic mirrors. If the probe signal is instead reflected from the sample, it is recollected and parallelized by a spherical mirror (100mm focal length), then redirected to the DPD input using a series of mirrors.

A micrometric translator is placed under a dielectric mirror (0° angle of incidence) used to direct the reference probe beam on the DPD (through another 45° AOI dielectric mirror). This way it is possible to adjust the optical path so that the two probe beams reach the DPD inputs at the same time and the noise band, caused by their otherwise offset arrivals, is minimized.

A picture of these two line configuration is reported in fig(5.4):

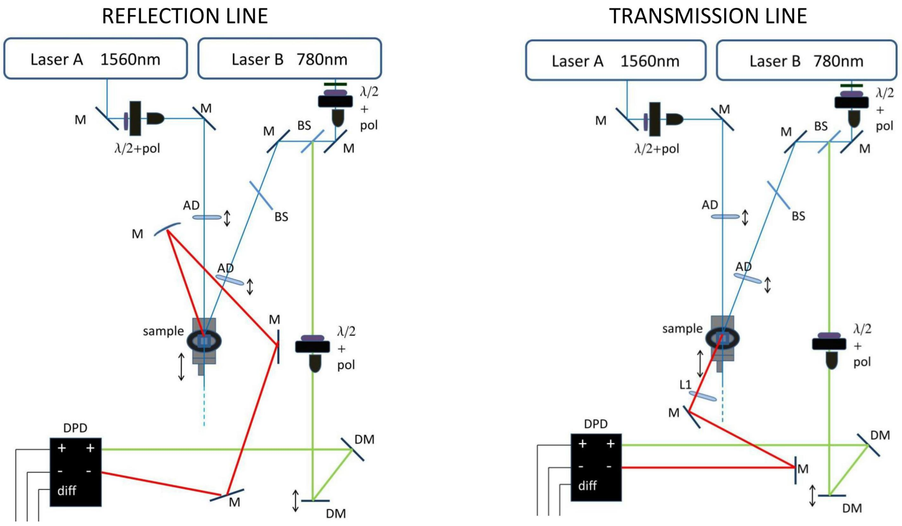
REFLECTION LINE

TRANSMISSION LINE

Figure 5.4: Scheme of reflection and transmission optical line. In both scheme the probe reference beam is in green and the probe beam coming from the sample is in red.

TRIGGER LINE: The pump laser beam is taken from the main line (sample line) using a mirror mounted on a tipper support, while the probe laser beam is partially extracted from the sample line using a 50:50 beam splitter. The beams are focalized by a 10 cm focal length lens and directed on a type I BBO non linear crystal. The spatial coincidence is obtained making the two beams contemporary passing through a 75 μm pinhole mounted on the sample support, then replaced with the crystal.

fine adjustment of the crystal position are made using a micrometric translator and phase matching condition is obtained via a graduate, finely regulable, manual rotator placed under the support. Once the pulse at 520nm is produced, it is detected by the APD and visualized on the oscilloscope. As mentioned before, this signal becomes a check for the trigger signal. Below is a picture representing this line configuration:

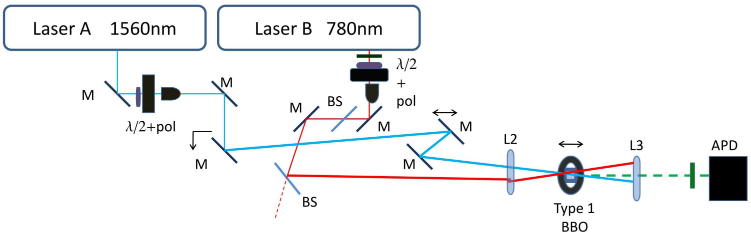

Figure 5.5: Scheme of the trigger line

5.2.2 Calibration and test measurements on HOPG

Before starting measurement sessions on BSLCO we performed a calibration of the rotator on which we mounted the $\lambda/2$ waveplate, placed to control the pump intensity and some test reflectivity measurements on HOPG (Highly Ordered Pyrolytic graphite) varying several pump fluences. We choose this material because its behavior is well known and it provides a relatively big signal for ΔR (of the order of 10^{-3}). The equation that regulates the intensity trend $I(\theta)$ as function of the angle θ at which the $\lambda/2$ waveplate is rotated is:

$$I(\theta) = I_0(cos^2(\theta) - sin^2(\theta))^2 \tag{5.2}$$

We placed a metallic removable mirror just after the combination $\lambda/2$ (on the rotator) + polarizer and deviates all the pump beam to an amplified photodetector to collect the signal at every single angle from 0 to 45 degrees. The result is shown in fig(5.6) representing our experimental values and the fit.As it is clear from the graphic, the intensity trend is in very good agreement with the fit, this assured us a linear change in the ΔR signal with respect to the fluence.

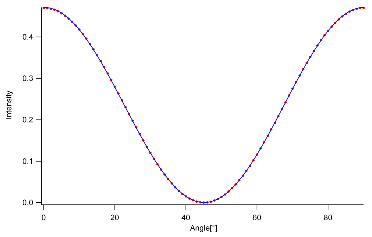

Figure 5.6: pump intensity vs. waveplate's angle. the red dots are the experimental data and the fit is in blue.

We now report some preliminary measurement we performed on HOPG varying the pump intensity, to show this linear relation:

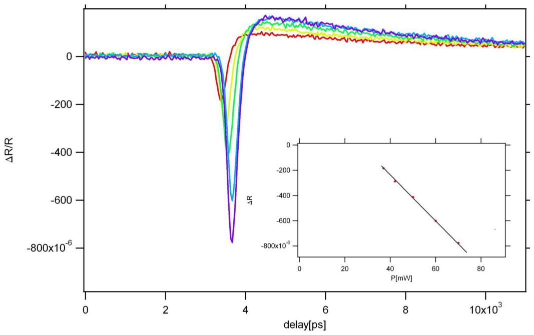

Figure 5.7: ΔR signal of HOPG at various pump intensities. In the small window, the linear trend between measured power an ΔR peak is shown.

We report the acquisition settings in table below:

Δf	50Hz
Sample rate	15MS/s
N° acquired points	15000
laser resolution	5 fs
PCI 5922 resolution	33.3 fs

Chapter 6

Measurements and data analysis

In pump-probe experiments, a pump pulse excites electrons above the Fermi level E_F and the probe pulse follows the relaxation dynamics of the system towards equilibrium. Conventional pump and probe experiments usually supply a transient response signal (reflectivity or transmittance variation) in a time window until few hundreds of picoseconds after the pump excitation. As explained in chapter 4 and 5, Asops technique enable the sampling of a whole 10 ns time window for each measurement, as it doesn't need and individual sampling for each point and doesn't need a mechanical delay stage. The study of a 10 ns transient response allowed us to observe a long relaxation dynamics which can be divided in three parts: a first, already known, dynamics concerning electron-phonon coupling mechanism which have an overall duration of few picoseconds. The successive part of the ΔR profile presents damped oscillations, having a period of tens of picoseconds, which starts right after the fast anharmonic decay and are visible until few nanoseconds after the pump excitation. The tail of the ΔR profile finally runs out with an exponential decay which represents the slow thermalization of the

system.
To make our presentation more clear, we will divide this chapter into two section: the first one concerning data on electron-phonon coupling in the section *fast dynamics* while the oscillating dynamics which partially overlap the slow exponential decay are grouped in the section *slow dynamics*.

6.1 Fast dynamics

In this section we report time resolved reflectivity measurements on BSLCO in the normal state for three different doping levels:

- optimally doped: $x = 0.4$, $p = 0.16$
- underdoped: $x = 1$, $p = 0.03$
- underdoped: $x = 0.8$, $p = 0.10$

All this measurements have been performed at T=290K. We acquired 20 measurements for each sample with the following set of acquisition parameters

Δf	50Hz
Sample rate	15MS/s
N° acquired points	8000
laser resolution	5 fs
PCI 5922 resolution	33.3 fs

We mediated this 20 twin measurements in order to significantly reduce noise (up to the order $\sim 10^{-6}$)

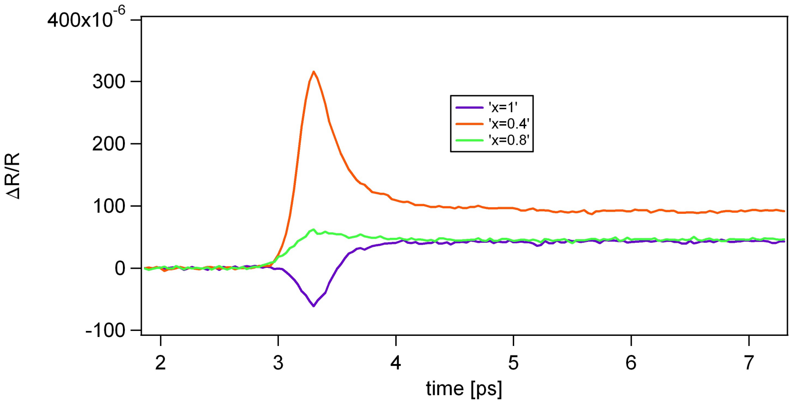

Figure 6.1: This measurements refers to the optimally doped (x=0.4) and the two underdoped (x=1, x=0.8). The three different samples exhibit a change in the ΔR signal changing from positive to negative.

In fig(6.1)we report a graph showing the observed change in the ΔR signal for the three samples obtained for the pump fluence of $186\mu J/cm^2$. The energy density for each sample is calculated by dividing the laser pump fluence for the respective penetration length and the values obtained are $3.59J/cm^3$ in the case of the optimally doped (OD04), $2.12J/cm^3$ and $2.04J/cm^3$ respectively in the case of underdoped with $x = 0.8$ (UD08) and underdoped with $x = 1$ (UD1). Higher incident powers of the pump beam on the samples were too offensive for the samples and caused the detected signal to become instable as a consequence of the sample damage. The underdoped sample with hole concentration $x = 0.8$ display a low ΔR signal as compared to the other two samples, for the reasons already explained in chapter 2. Therefore, we were able to perform other measurements decreasing the pump fluence only for the optimally doped $x = 0.4$ and underdoped $x = 1$ BSLCO.

From the picture we can observe that all ΔR profiles deliver two different dynamics involving the fast relaxation dynamics of electrons and the first subset of hot phonons (with decay time of the order of hundreds of femtoseconds) and slow relaxation dynamics of this first subset reaching the equilibrium with the rest of the lattice (with a decay time of the order of few picoseconds). We also observe, as mentioned in chapter 3, that the fast dynamics change their sign from positive to negative as passing from the optimally doped to the underdoped (UD1), this fact has an electronic origin as this first decay time is related to changes in the electronic temperature T_e. The slow dynamics, related to lattice temperature, are instead unchanged.

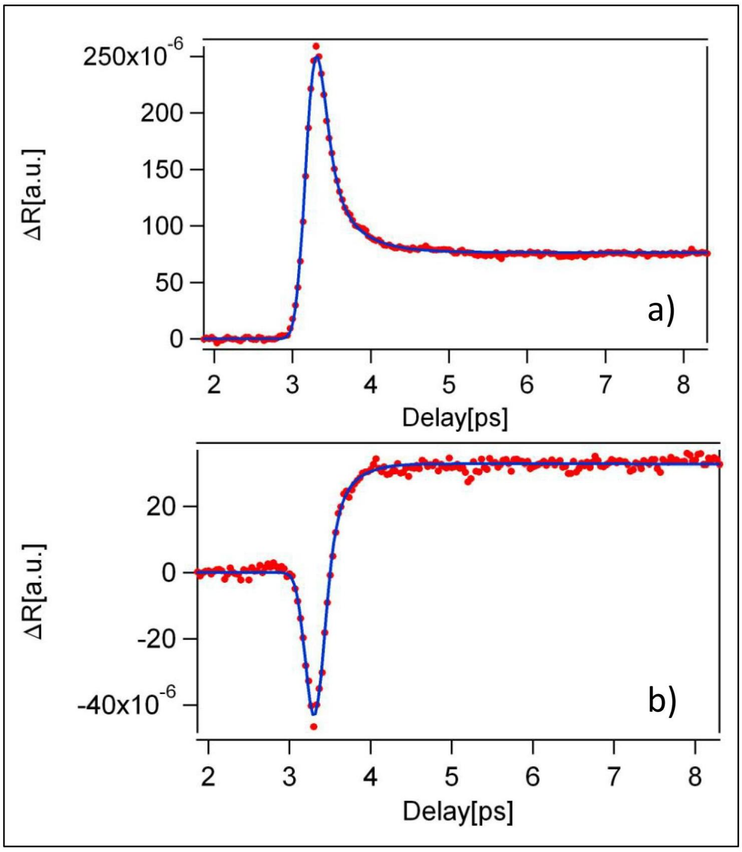

Figure 6.2: experimental data (red dots) and correspondent fit are reported for OD04 (a) and UD1 (b)

We fitted our measurements using the three temperature model (see chapter 2) in order to extract the values of λ, τ_h and f for each doping level. The

3TM equations (2.8,2.9,2.10) were integrated in order to obtain the temperature profile of electrons T_e, hot phonons T_p and cold phonons (the rest of the lattice) T_l, the reflectivity variation profile was then fitted using equation2.4. From the graph in fig.(6.1) it is clear that the ΔR signal obtained was too low and affected by noise, thus we were not able to get an acceptable fit. We instead report in fig.(6.2) the fit obtained for the other two samples and our results:

x	$\Omega_0[meV]$	λ	f	$\tau_h[ps]$
0.4	70	0.060 ± 0.01	0.08 ± 0.01	0.3 ± 0.01
1.0	70	0.10 ± 0.01	0.09 ± 0.01	0.6 ± 0.01

We used the same phonon frequency Ω_0 used by[7]and[9], the pulse width, evaluated as explained in chapter 5 and appendix, is 248 fs.

Our results are consistent with values reported in literature[10] and comparing the optimally doped with underdoped UD1 we observe that, the values of correspondent λ increases for the last one.

From measurements performed on optimally doped BSLCO varying the incident pump intensity we could verify that λ does not depend on the fluence. We report an example in fig. (6.3), for a pump fluence of $121 \mu J/cm^2$ we still measured $\lambda = 0.06 \pm 0.01$.

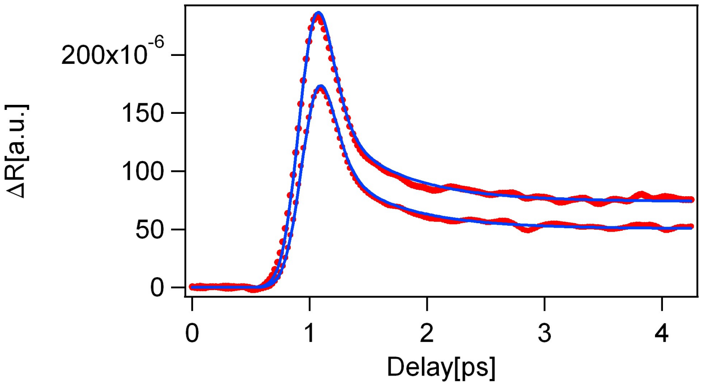

Figure 6.3: two differen ΔR profiles of the OD04 for two different pump fluences and correspondent fits.

6.2 Slow dynamics

As outlined at the beginning of this chapter, extracting the relevant physical information from pump-probe reflectivity measurements made with ASOPS turned out to be quite challenging: measurements of reflectivity variation of BSLCO performed in a 10 ns measurable time window delivered, beside the experimental data displayed in the former section, an interesting slow relaxation dynamics of the system consisting in damped oscillations occurring just after the anharmonic decay peak and lasting for few hundreds of picoseconds. This oscillations occur for all the three samples but are more definite for the OD04 and UD1 crystals. They have a period of some tens of picoseconds, their amplitudes decrease with the lowering of the pump fluence and presents acoustic frequencies. We report our measurements and acquisition settings for the OD04 and UD1 BSLCO in fig.(6.4). As already outlined in the previous section, the measurements on the UD08 BSLCO were quite noisy and we report them in fig. (6.5)

OD04-UD1 BSLCO	
Δf	33Hz
Sample rate	15MS/s
N° acquired points	8000
laser resolution	3.3 fs
PCI 5922 resolution	22 fs

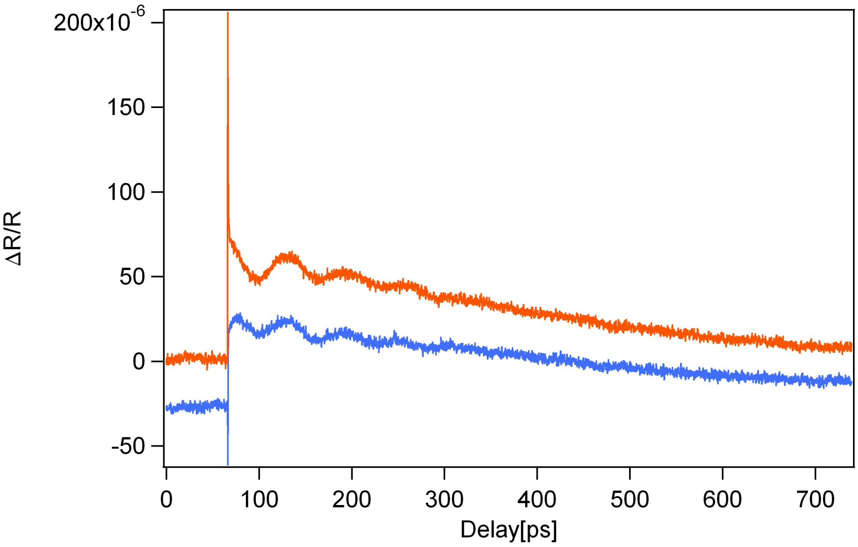

Figure 6.4: Oscillatory dynamics delivered by OD04 (orange) and UD1 (blue) BSLCO.

UD08 BSLCO	
Δf	1KHz
Sample rate	15MS/s
N° acquired points	30000
laser resolution	100 fs
PCI 5922 resolution	666.6 fs

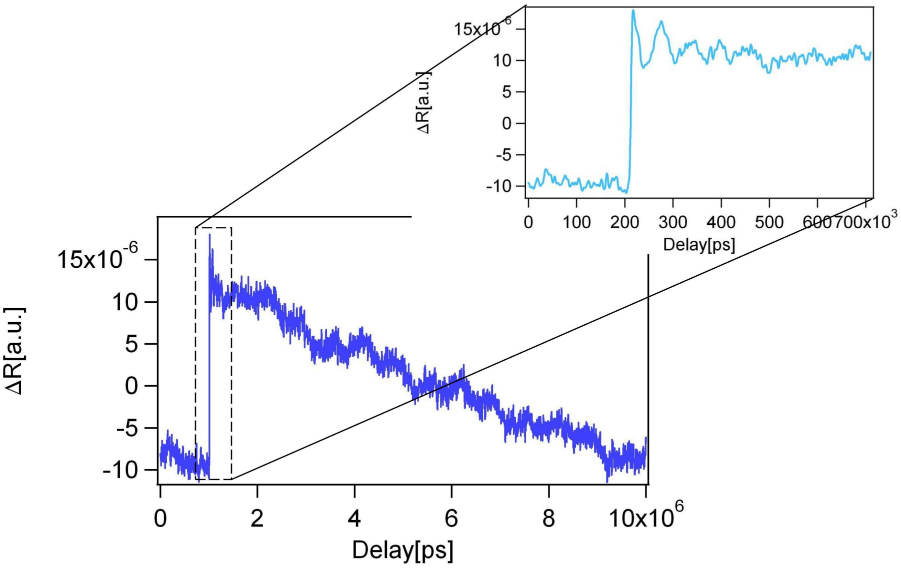

Figure 6.5: Complete dynamics delivered by UD08. The blow up window on the right top delivers the oscillatory dynamics.

Comparing the graph reported in the above figures, it is clear that the noise affecting the measurements on the UD08 sample prevented us to visualize the oscillations, the ratio between noise and the amplitude of the first period being ~ 0.6. We then focused on OD04 and UD1.

Similar oscillations have been observed by Mansart et al.[3] in studying the effects contributing to the ultrafast response of vanadium sexquioxide across the metal-insulator transition. At time scales of some tens of picoseconds they could observe oscillations which they attributed to the propagation of a coherent acoustic wave, since its frequency corresponds to a wave with the same wavelength as the laser pulse but traveling at the velocity of sound in the compound.

The excitation of coherent acoustic waves by an ultrashort laser pulse was phenomenologically described by Thomsen[12]. The detection of coherent acoustic waves in a pump-probe reflectivity measurement can be explained as a Brillouin scattering phenomenon occurring in the system after excitation of the wave by the pump pulse. The scattering condition is

$$q_{ph} = 2nk_{probe} \cos \theta_i \tag{6.1}$$

where q_{ph} is the phonon wave vector, n the real part of the refractive index and the probe photon has a wave vector k_{probe} arriving at incident angle θ_i with respect to the normal surface. Following this scattering condition, the probe beam acts as a filter to select the acoustic wave propagating along the scattering plane symmetry axis, i.e. the normal to the sample surface, and traveling with the wave vector q_{ph}.

Currently we haven't carried out a sufficiently accurate study to draw effective conclusions, but we can make some considerations and hypothesis on the base of the elements extracted by fitting our data with the following test function:

$$f(t) = A \sin [(\omega + B(t - t_0))(t - t_0) + \phi]e^{-C(t-t_0)} + Ie^{-\frac{t-t_0}{\tau}} + D \tag{6.2}$$

In the first term we have assumed a sine behavior of the oscillating part, with amplitude A and frequency linearly varying with the period. The first exponential takes into account the damping of the oscillations through the C factor, the second exponential factor keeps into account the slow exponential decay of the system, t_0 is the initial time fixed for every measurement and D is an offset constant. We have fitted function 6.2 obtained for 8 different fluences of the optimally doped sample and 5 different fluences of the underdoped sample in order to establish wether and how the fit parameters A, ω, B, C depend on the laser fluence. We report the measurements and fits in fig. (6.6)

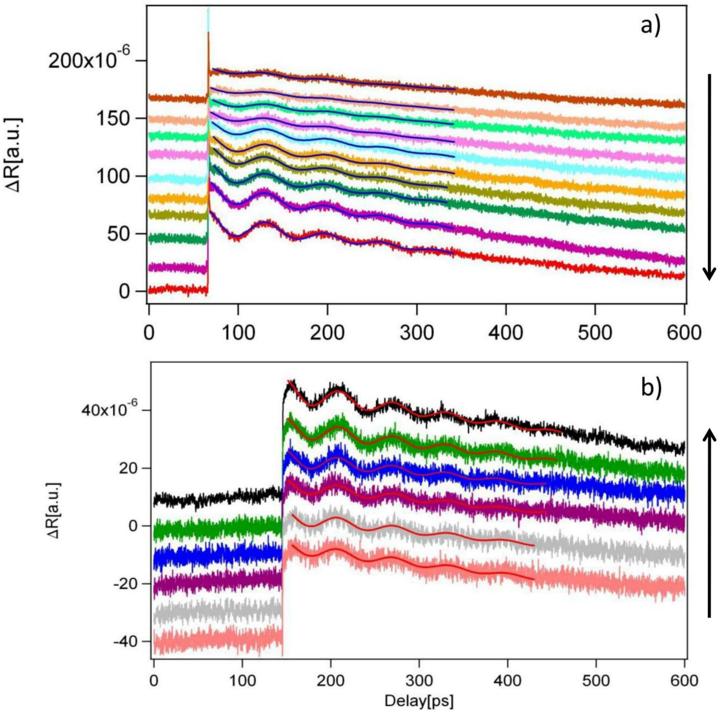

Figure 6.6: measurements and fits of OD04 (a) and UD1 (b). Arbitrary offsets has been added to the different measurements.

With respect to the above graphs, we report the energy density values for each trace in the order indicated by the black arrows and the corresponding extracted fit parameters:

OD04 (fig. 6.6a)

$E[J/cm^3]$	$A[\cdot 10^{-5}]$	ω	$B[\cdot 10^{-5}]$	C
3.59	2.27	0.081	4.08	0.009
3.09	2.16	0.077	4.78	0.010
2.59	2.10	0.081	3.61	0.011
2.34	1.67	0.083	2.63	0.011
2.10	1.52	0.079	3.42	0.010
1.87	1.17	0.073	5.22	0.009
1.24	1.10	0.061	8.99	0.012
1.05	1.03	0.057	10.04	0.012

UD1 (fig. 6.6b)

$E[J/cm^3]$	$A[\cdot 10^{-5}]$	ω	$B[\cdot 10^{-5}]$	C
2.04	1.22	0.093	1.70	0.007
1.75	1.01	0.092	2.03	0.007
1.47	1.06	0.090	2.34	0.008
1.33	0.77	0.081	3.63	0.007
1.19	0.78	0.098	0.10	0.007

To evaluate the accuracy of the values obtained by the fit, we tested their sensibility with respect to the variation of the other parameters. All the values reported of A and B presented variations on the order of 10^{-7} while ω and C display variation on the order of 10^{-3}. The fit parameters A, ω, B and C trend is reported in fig. (6.7) as function of the energy density:

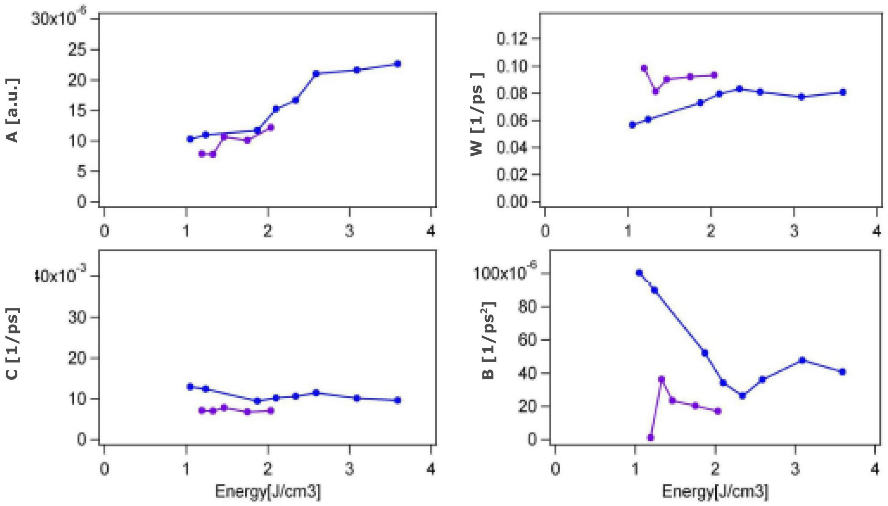

Figure 6.7: Fit parameters trend are reported for OD04 (blue) and UD1 (violet) as function of the energy density.

We also report the trend of the phase ϕ for both samples. The phase seems to be constant around value of 0.1 which validate our choice to use a sine function in the fit:

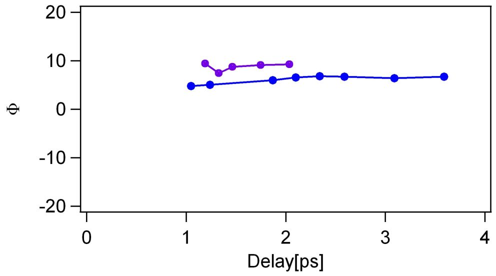

Figure 6.8: phase trend as function of the energy density for OD04 (blue) and UD1 (violet)

The last set of measurements analysis concern the relaxation dynamics towards equilibrium of the cold lattice τ_c. We then report measurements and fits concerning the slow exponential decay time for the OD04 and UD1 at various fluences together with acquisition settings (the same for both samples):

Δf	1KHz
Sample rate	15MS/s
N° acquired points	30000
laser resolution	100 fs
PCI 5922 resolution	666.6 fs

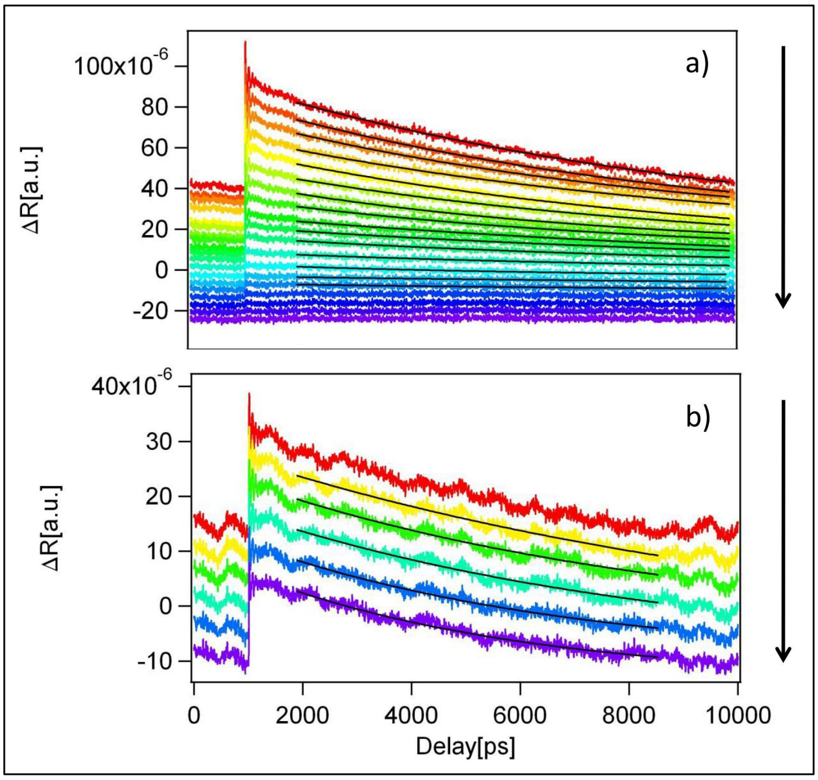

Figure 6.9: measurements and fits concerning the low exponential decay time for the OD04(a) and UD1 (b) at various fluences. The black arrows indicate the fluence trend.

In table below we report the energy densities and values of τ:

OD04 (fig. 6.9a)		UD1 (fig. 6.9b)	
$E[J/cm^3]$	$\tau[ps]$	$E[J/cm^3]$	$\tau[ps]$
3.59	1070	2.04	1190
3.09	1200	1.75	8400
2.59	1240	1.47	1260
2.34	1170	1.33	1260
2.10	1170	1.19	1690
1.87	1190		
1.24	1480		
1.05	1320		
0.87	980		
0.71	1130		
0.44	1150		
0.32	1640		
0.23	710		
0.15	1230		

We then report the trend of τ_c as function of the energy density. As it can be seen in fig.(6.10) this slow decay time remains constant with variation of the energy density for both OD04 and UD1.

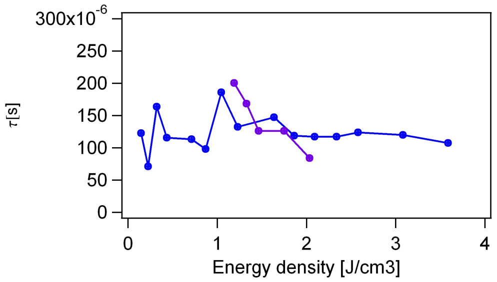

Figure 6.10: τ_c as function of the energy density for OD04(blue) and UD1 (violet)

Chapter 7

Discussion and conclusions

In our experiment we investigated the optical properties of HTSC out of equilibrium with pump-probe technique performed with ASOPS obtaining information concerning a fast dynamics and a slow dynamics. In chapter 6 we reported our results and analysis. We will now report our results as function of the dopant carriers concentration for the OD04 and UD1 to show how this affects the system's behavior out of equilibrium of BSLCO:

7.1 Quantities related to the electron-phonon coupling: λ and τ_c

As mentioned in chapter 1, we do not expected λ to be higher than its common values obtained in the case of metals and, according to [13] we expected λ to be higher in the case of underdoped BSLCO than in the case of optimally doped. We report in fig.(7.1) predictions by [13] and our results:

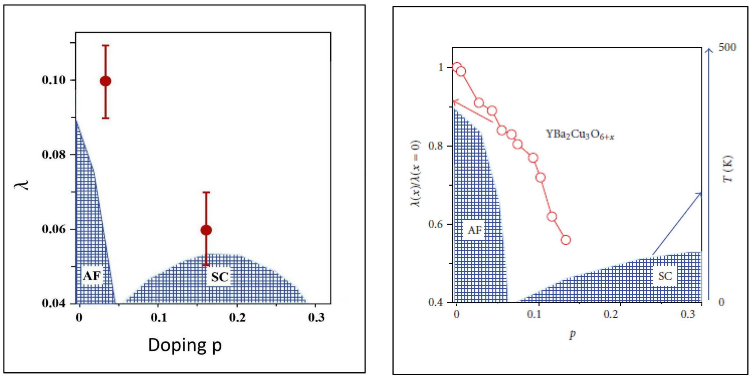

Figure 7.1: electron-phonon coupling constant λ as function of real doping p. The right picture is taken from[13]

theoretically, the decrease of λ with the doping is explained with the appearance of polarons.

We have to point out that in the case of the studies conduced by[13], λ takes into account the interaction between electrons and the whole set of phonons while in our case, λ represent the coupling strength between electrons and a subset of hot phonons which first interact. The comparison is anyhow significant, and we can conclude that λ is not the only factor to account in sorting out the mechanisms at the base of the superconductive phase in HTSC.

The slow decay time τ_c does not vary with respect of the fluence, we can report its average value for both samples as function of the doping (fig. 7.2. We can conclude that this slow decay time is not significantly affected by the doping.

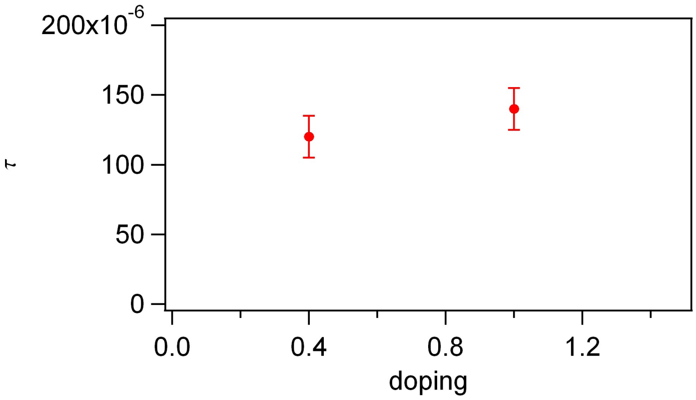

Figure 7.2: Avarage τ_c as function of doping.

7.2 Oscillatory dynamics

We observed an oscillatory dynamics on the scale of some tens of picoseconds which might be ascribed to the propagation of a coherent acoustic wave, but we cannot draw a definitive conclusion, because of the lack of other experimental proofs, for example it would be useful to observe these oscillations for different probe colors. However we can discuss the results we have obtained comparing them for different values of doping. The frequency ω of the oscillations seems to vary with the energy density, at least at low values of this one (fig. 6.7), we then report in fig.7.3a) the values of two different frequencies values as function of doping for similar energy densities in the two samples ($\sim 2\ J/cm^3$ and $\sim 1.2\ J/cm^3$ respectively). The damping factor C seems to be constant with respect to energy density so we decided to report in fig. 7.3b) the values of its average as function of doping.

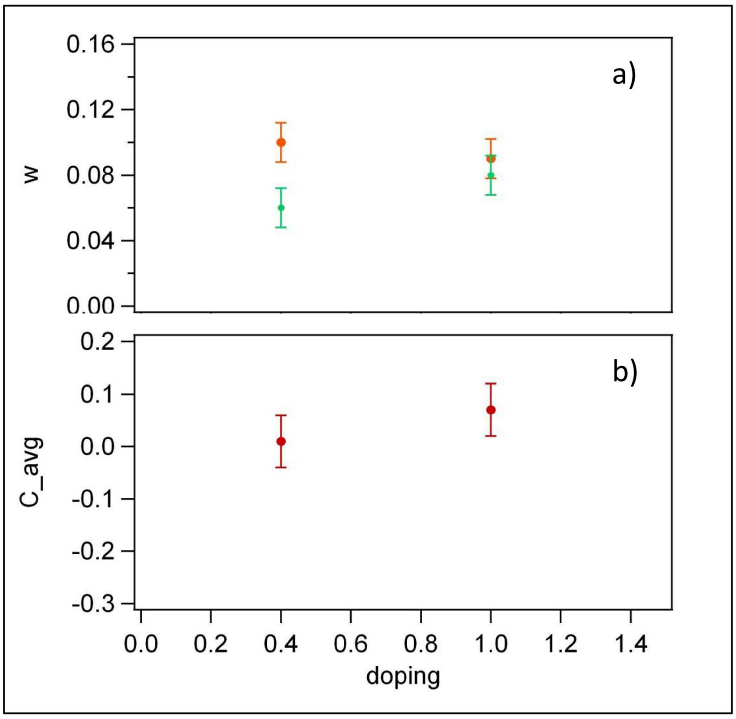

Figure 7.3: (a) the orange dots represent two frequencies values as function of doping for similar energy densities at $\sim 2J/cm^3$ (orange dots) and $\sim 1.2J/cm^3$ green dots). In figure (b) we report the values of the average damping C as function of doping.

From these graphs we can say that the oscillation frequency ω seems to increase with the doping for low fluences and decrease with the doping at higher fluences, while the damping factor C does not seem to be significantly affected by the fluence.

Appendix

LIST OF EMPLOYED OPTICAL ELEMENTS (referred to fig. 5.3):

metallic mirror

We used both silver and golden plane mirrors (M). Their average reflection is around 98% for a wavelength range of 450-2000 nm.

spherical mirror

We used a silver coated concave mirror (f=100 mm) to recollect and parallelize the probe beam reflected from the sample. These devices are commonly used in broadband applications in the visible, NIR, or IR to collect, focus, or image light since they do not introduce chromatic aberration during this process. For such mirrors $f = R/2$ where R is the radius of curvature of the mirror.

dielectric mirrors

We used two dielectric mirrors (DM) to reflect the probe beam. the first one is a 0° AOI DM and the second one is a 45° AOI DM. These devices have a fused silica substrate and multilayer coatings are stacked intended to achieve the highest possible reflectivity at specific laser wavelengths at normal or 45 degrees incidence. Their reflection is $> 99\%$

beam splitter

We used two plate beamsplitters (BS), the first is a 70:30 BS, the second is a 50:50 BS. These devices have a coated front surface that determines the beam splitting ratio while the back surface is wedged and AR coated in order to minimize ghosting and interference effects.

achromatic doublets

This devices significantly reduce chromatic aberration and have a superior optical performance to singlet lenses, the spot from a doublet is 4-5 times smaller than a singlet lens spot. We used a NIR achromatic doublet (650-1050 nm) to focalize the 780 nm beam (f=50 mmm, reflectivity at 800 nm=30%) and a IR achromatic doublet (1050-1620 nm) to focalize the 1560 nm beam (f=100 mm, reflectivity at 1600 nm=10%)

lenses

The lenses we employed in our set up are uncoated plano-convex lenses: L_1 has f=50mm, L_2 and L_3 have f=100 mm, they transmits more than 90% of the beam both at 800 and 1600 nm.

$\lambda/2$ **waveplates**

Waveplates are made from materials which exhibit birefringence. The velocities of the extraordinary and ordinary rays through the birefringent material varies inversely with their refractive indices. This difference in velocities gives rise to a phase difference when the two beams recombine. A linearly polarized beam incident on a half wave crystal quartz waveplate emerges as a linearly polarized beam but rotated such that its angle to the optical axis is twice that of the incident beam.

BBO crystal

$\beta - BaB_2O_4$ non linear crystal. Transparency range: 189-3500nm, dimensions: 10x10x0.5 mm, phase-matching angle at 15° (da ricontrollare)

DIFFERENTIAL PHOTODETECTOR:

The detector we employed in our experience is a balanced amplified photodetector that consists of two well-matched photodiodes and an ultra-low noise, high-speed transimpedance amplifier (TIA) that generates an output voltage (RF OUTPUT) proportional to the difference between the photocurrents in the two photodiodes (i.e., the two optical input signals). Additionally, the unit has two fast monitor outputs (MONITOR+ and MONITOR-) to observe the optical input power levels on each photodiode separately by connecting them to the oscilloscope. These outputs are low frequency outputs and cannot be used to measure an RF modulation on the signal.

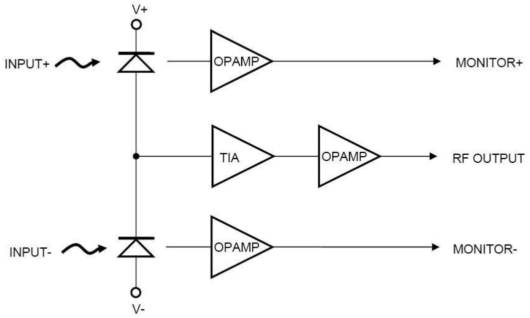

Figure 7.4: electronic scheme of the detector

SPECIFICATIONS:

Detector type	Si/PIN
Wavelength range	320-1000 nm
active detector diameter	0.3 mm
bandwidth (3dB)	DC-100MHz

AUTOCORRELATION OF GAUSSIAN PULSES

Let us consider two gaussian pulses, like our laser pulses, with intensity $I_1(t)$ and $I_2(t-\tau)$. They interact with the nonlinear crystal with a transmission frequency proportional to their intensity product:

$$R(\omega, t, \tau) = \sigma(\omega) I_1(t) I_2(t-\tau) \tag{7.1}$$

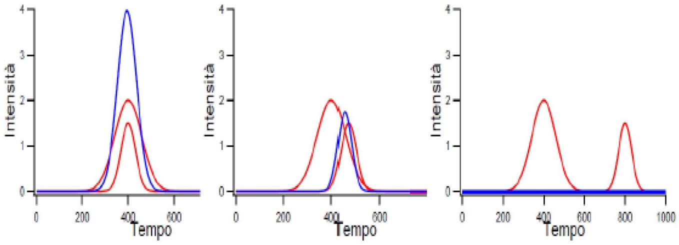

Figure 7.5: Temporal evolution of the sum frequency signal vs. delay

The convolution of these two signals is maximum when they are in temporal coincidence (the gaussians completely overlap, see fig7.5, first graph), and reduces as long as the temporal distance increases (the overlap decrease until it vanishes, see fig7.5, second and third graph). Therefore the transmitted signal depends on the time delay (τ) between the two pulses:

$$A(\tau) = \int_{-\infty}^{+\infty} I_1(t) I_2(t-\tau) dt \tag{7.2}$$

Since we are considering gaussian pulses, their expression is:

$$I_1(t) = I_1 e^{-\frac{(t-t_1)^2}{2\sigma_1^2}} \qquad I_2(t) = I_2 e^{-\frac{(t-t_2)^2}{2\sigma_2^2}} \tag{7.3}$$

The convolution of two gaussian pulses of width σ_1 and σ_2 respectively is still gaussian:

$$A(\tau) = I_1 I_2 \int_{-\infty}^{+\infty} I_1(t) I_2(t-\tau) dt \tag{7.4}$$

which gives

$$A(\tau) = I_1 I_2 \sqrt{2\pi} exp - \frac{r^2}{2(\sigma_1^2 + \sigma_2^2)^2} \tag{7.5}$$

This is a gaussian of width $\sqrt{(\sigma_1^2 + \sigma_2^2)}$

Bibliography

[1] P.B. Allen *Theory of Thermal Relaxation of Electrons in Metals*, Phys. rev. lett. 59:1460,1463

[2] S.D.Brorson *Femtosecond Room-Temperature Measurements of the Electron-Phonon coupling constant λ in Metallic Superconductors*, Phys. rew. lett. 64, 18:2172,2175

[3] B.Mansart *Mott transition in Cr-doped V_2O_3 studied by ultrafast reflectivity: Electron correlation effects on the transient response*, EPL 92 (2010) 37007: p1,p6

[4] Menlo System, *ASOPS white paper*, April 15 2009

[5] Menlo System, *User Manual*, 9:section 4, Giuly 2009

[6] S. De Cesari, *Misure di autocorrelazione e assorbimento a due fotoni mediante campionamento ottico asincrono*, January 2011

[7] S. Dal Conte, *time-resolved optical spectroscopy on* $Bi_2Sr_2Ca_{0.92}Y_{0.08}Cu_2O_{8+\delta}$, March 2011

[8] G. Coslovich *Dinamiche di non-equilibrio foto-indotte e possiili effetti di transizione di fase in superconduttori ad alta temperatura critica*, 2006

[9] L.Perfetti et al. *Ultrafast Electron Relaxation in Superconducting* $Bi_2Sr_2Ca_{0.92}Y_{0.08}Cu_2O_{8+\delta}$ *by Time-Resolved Photoemission Spettroscopy*, phys. rev. lett. PRL99,197001:1,4, 2007

[10] S.Lupi et al. *Far-infrared Absorption and Metal-to-Insulator Transition in the Hole Doped Cuprates*, phys. rev. lett.PRL102, 206409: 1,4, May 2009

[11] F.F. Balakirev *Magneto-transport in LSCO* $high - T_c$ *superconducting thin films*, New J. phys, 8(2006)194:912,914

[12] C. Thomsen, *Surface Generation and Detection of Phonons by Picosecond Light Pulses*, Phys. rew. B, vol.34 n 6,4129-4138

[13] A.S. Mishchenko *Manifestations of the Electron-Phonon Coupling in the Spectroscopy of High-Temperature Superconductors*, Hindawi Publishing Corporation, vol. 2010, ID 306106

Ringraziamenti

Questo paragrafo è dedicato a ringraziare alcune persone, a me molto care, che mi hanno dato una mano nello svolgimento di questo lavoro. Mi sento di ringraziare, innanzitutto, una persona in particolare: Claudio. Grazie per avermi seguito durante tutto l'iter, dai primi passi in laboratorio, alla stesura finale, con grandissima competenza, con pazienza, con molti consigli utilissimi e una disponibilità che pochi professori sono in grado di offrire, nonostante i tuoi mille impegni. Ringrazio vivamente anche il professor Ferrini, per aver reso possibile l'attuazione di questo lavoro, per la disponibilità e la gentilezza che dimostra sempre quando ha a che fare con noi studenti.

Un grossissimo ringraziamento va ai miei genitori, che mi hanno sempre sostenuto, in tutti i sensi, con grandissimo affetto, hanno saputo guidarmi in tutti questi anni, ma mi hanno sempre permesso di scegliere, vi voglio bene!

Ci sono altre persone a cui devo dei ringraziamenti particolari: Federico, per il suo aiuto in laboratorio, Stefano per il suo aiuto con i fit e il mio grande compagno Simone, che ha condiviso con me mesi di laboratorio, con radio italia a manetta, tutti i momenti divertenti e soddisfacenti, ma anche quelli frustranti, in cui non funzionava nulla!

Ringrazio anche tutti gli amici che mi sono stati vicino, mi hanno incoraggiato e aiutato, ognuno a modo suo e con i propri mezzi: Andrea, Fabrizio, Davide, Marina, Paolo, Matteo, Giulia e Stefano.

Ringrazio tutti i compagni e i professori che ho incontrato durante questi anni di università perchè hanno contribuito alla mia formazione, sia scien-

tifica, sia personale. Un ultimo ringraziamento particolare, infine, va a Dadi, per l'incredibile supporto, pratico ed emotivo, perchè sei sempre stato presente e perchè da quando ci sei tu, tutto ha acquistato un sapore diverso.